SIBYL

(SeIsmic monitoring and vulnera**B**ilit**Y** framework for civi**L** protection)

Agreement number: ECHO/SUB/2014/695550

Deliverable DB1: Guidelines for the remote-sensing assessment methodology

Version 1 February 2016

Project start date: 01.01.2015 End date: 31.12.2016

Coordinator: Prof. Dr. Stefano Parolai

Centre for Early Warning Systems

Helmholtz Centre Potsdam GFZ German Research Centre for Geosciences, Potsdam, Germany

Contents

Introduction

The aim of this document is to guide and assist a non-skilled user in the process of collecting, processing and interpreting remote-sensing data within the framework of exposure and vulnerability assessment.

Remote sensing for vulnerability-centred investigations is a less established field of research than other uses of remote sensing, and other means of undertaking vulnerability assessment. Nevertheless, a vast amount of research has been undertaken with the aim of deriving pre-event vulnerability indicators that are related to physical, demographic and socioeconomic aspects of vulnerability by the exploitation of remotely-sensed imagery.

In order to provide simple, but effective tools to civil protection authorities, within the SIBYL project simpler approaches have been preferred to sophisticated solutions, which while providing very accurate results are also bound by complex operational settings and are strongly dependent on the expertise of the users.

As part of this, a simple plug-in for the well-known Quantum GIS (QGIS) GIS platform[1], termed SATEX (SATellite EXposure information extraction), has been implemented to carry out a supervised land-use / land-cover (LULC) assessment using medium resolution multi-spectral images. LULC provides a useful partitioning of an area of interest into classes which represent the basic attributes of the territory in question, and whose knowledge can therefore be exploited to drive any subsequent in-situ data collection activity.

Focusing on medium resolution, multispectral Landsat[2] imagery is based on the following considerations:

- Landsat is available globally, free of cost, and the most recent sensors feature a geometric resolution adequate for different operational scales, ranging from the block-scale to the regional scale.
- Despite the geometric resolution being significantly lower than some commercially available products, such those commonly visible in the Google Map applications, the information contained in the multiple spectral bands provides a very rich content which can be more efficiently exploited by the statistical learning approaches implemented in the software.

In the following sections, an introduction to remote sensing for geo-risk issues is given, including a discussion about the value of medium-resolution imagery and data sources (in particular focusing on the Landsat products) and the Sentinel series of space missions which will provide great opportunities for exploiting remote sensing in vulnerability assessment. Next, a complete set of guidelines for the use of the SATEX plugin is provided.

[1] http://www.qgis.org/en/site/
[2] http://landsat.usgs.gov/

Remote sensing in geo-risk analysis

Within the context of geo-risk analysis, for both the pre- and post-event phases, as well as hazard- and vulnerability-centred investigations, past- and present-day remote sensing missions have proven useful. Data with a coarser geometric resolution and larger spatial coverage per scene are able to contribute to the overall evaluation of pre- and post-event situations. In contrast, it is still both difficult and expensive to obtain high geometric resolution data such as airborne LIDAR or VHR (very high resolution) optical data over larger areas affected, specifically in the case of an earthquake event (Rathje and Adams, 2008). In addition to that, the geometric resolution of the sensors and the associated scene size and thus, the spatial scale of analysis, need always to be selected in consideration of the context of the objects to be analysed. For instance, coarse resolution remote sensing data can be utilized to accurately analyse large-scale phenomena and objects such as large active faults or mass movements. In contrast, vulnerability-related evaluations of small-scale objects such as buildings may only lead to a rough estimation based on such data.

Future earth observation missions have the potential to play a key role in earthquake- and landslide-related investigations and to continue or even improve upon existing geoinformation products. For example, the ESA Sentinel[3] missions currently being developed and launched will feature enhanced geometric and thematic capabilities and increased revisit capabilities at a low cost (see the section below). Other current and future missions, such as ALOS-2[4], the Radarsat[5] constellation, DESDynI[6], CARTOSAT-3[7], ALOS-3, TerraSAR-X 2, TanDEM-L[8], WorldView-3[9], as well as the hyperspectral sensors EnMAP[10] and HyspIRI[11], still need to be assessed in terms of cost and applicability with respect to the particular research questions being addressed. For example, TanDEM-L will open up opportunities to better understand the Earth's dynamic surface processes, enabling the continuous monitoring of earth surface deformation, e.g., due to seismic movements, volcanic eruptions, landslides, subsidence or uplift within the range of centimetres. In this context, the enhanced capabilities of the described missions are believed to enable a leap forward in earthquake and landslide risk research both for hazard- as well as vulnerability-related investigations.

Apart from these current and future perspectives, international research groups from both governments and academia have produced remote sensing based geo-products in past years that will provide valuable input to vulnerability-related research within the context of the SIBYL project. These include, on the one hand, large area global or regional land cover datasets that can be used as a first approximation of human and physical exposure as well as for the disaggregation of population census data. However, with regards to these products, a better understanding of each data set's strengths and weakness is still on demand. On the other hand, space-based pre-operational emergency response services have produced a large product portfolio and significant

[3] http://www.esa.int/Our_Activities/Observing_the_Earth/Copernicus/Overview4
[4] http://global.jaxa.jp/projects/sat/alos2/
[5] http://www.asc-csa.gc.ca/eng/satellites/radarsat/
[6] http://decadal.gsfc.nasa.gov/desdyni.html
[7] http://bhuvan.nrsc.gov.in/bhuvan/content/indian-remote-sensing-satellites-earth-observation-india-high-resolution-satellite-data
[8] http://www.dlr.de/hr/en/desktopdefault.aspx/tabid-8113/
[9] http://www.satimagingcorp.com/satellite-sensors/worldview-3/
[10] http://www.enmap.org/
[11] https://hyspiri.jpl.nasa.gov/

experiences in post-event mapping applications in recent years (e.g., the Copernicus[12] program, formerly known as the Global Monitoring for Environment and Security Programme, GMES, of the European Space Agency).

Throughout the rest of this report, applications and the presented sensor groups and the associated data sets will be related to the particular spatial scale of analysis at which they would be employed, which mainly depends upon the sensor-specific geometric resolution. The categorization of the spatial scale of analysis is based on the scheme presented by Neer (1999) and can be brought in line with the categorization suggested by GMES (2011) (Table 1). For reasons of lucidity, the number of classes was limited to five, namely “very high resolution (VHR)” (consisting of classes “extremely high resolution”, “super high resolution” and “very high resolution”), “high resolution”, “medium resolution”, “coarse resolution” and “very coarse resolution” (consisting of the classes “very coarse resolution” and “extremely coarse resolution”).

Table 1: Categorization of sensor-specific geometric resolution (Neer, 1999; GMES, 2011)

Neer (1999)		**GMES (2011)**	
Geometric resolution (m)	***Nomenclature***	***Geometric resolution (m)***	***Nomenclature***
0.05-0.25	Extremely high resolution	<=1	Very high resolution 1 (VHR1)
0.25-0.5	Super highresolution	1-4	Very high resolution 2 (VHR2)
0.05-1.0	Very high resolution	4-10	High resolution 1 (HR1)
1-4	High resoltion	10-30	High resolution 2 (HR2)
4-12	Medium resolution	30-100	Medium resolution 1 (MR1)
12-50	Coarse resolution	100-300	Medium resolution 2 (MR2)
50-250	Very coarse resolution	>300	Low resolution (LR)
>250	Extremely coarse resolution		

A comprehensive overview of the selected satellite platforms and sensors is given in Table 2, including the particular sensor specifications such as geometric resolution, swath width, and revisit capability. A categorization of the spatial scale of analysis is introduced based on the aerial coverage, i.e., the swath-width-dependent scene size, and the geometric resolution of the sensors according to the scheme presented by Neer (1999) and adopted by Geiß and Taubenböck (2013) for optical sensors. Being aware that, for example, SAR (Synthetic Aperture Radar) data do not contain the same thematic information as optical data with the same geometric resolution, the categorization is adapted also for non-optical sensors for sake of consistency. The categorization ranges from ‘‘focal’’ to ‘‘local’’ to ‘‘regional’’ to ‘‘national’’ scales of analyses, however, some of the sensors falling under the category “national” also allow ‘‘continental’’ or even ‘‘global’’ analysis.

[12] http://www.esa.int/Our_Activities/Observing_the_Earth/Copernicus

Table 2 Overview of several present-day optical and SAR remote sensing systems employed in earthquake and landslide risk analysis (Source: Categorization of analysis scales from Geiß and Taubenböck, 2012; most sensor characteristics from Joyce et al., 2009a, b and eoPortal, 2013; Characteristics for "Airborne LIDAR" from Rathje and Adams, 2008, for TanDEM-X from DLR, 2010, for Deimos-1 from ESA, 2012).

Spatial scale of analysis (associated sensor groups according to Neer, 1999)	Platform/Satellite	Sensor/Mode	Geometric resolution (Nadir) [m]	Swath [km]	Revisit capability
focal *(VHR / HR optical; VHR / HR SAR)*	**Airborne**	LiDAR	0.5-1	daily coverage of 1-100 km²	Mobilized to order
	Worldview-1/2	Panchromatic	0.46	16.4	1.1 days
		Multispectral	1.85		
	GeoEye-1	Panchromatic	0.4	15	<= 3 days
		Multispectral	1.6		
	Pleiades	Panchromatic	0.5	20	1-2 days
		Multispectral	2.8		
	Quickbird	Panchromatic	0.6	16.5	1.5-3 days
		Multispectral	2.4		
	Ikonos	Panchromatic	1	11	1.5-3 days
		Multispectral	4		
	Cosmo-Skymed	Spotlight	<1	10	~37 hours
	Formosat-2	Panchromatic	2	24	1 day
	TerraSAR-X	Spotlight	1	10	11 day repeat cycle;
	TanDEM-L	Stripmap	3	30	2.5 day revisit capability
	EROS A	Panchromatic	1.9	14	10.5 days
	EROS B	Panchromatic	0.7	7	6 days
	IRS-P5	Panchromatic	2,5	26-30	5 days
	IRS-P6	LISS-4	5.8	24	5 days
	ALOS	PRISM	2.5	70	Several times per year as per JAXA acquisition plan
	Radarsat-2	Ultra-fine	3	20	Every few days
local *(MR optical; MR SAR)*	**SPOT-1/2/3**	PAN	10	117	1-4 days
		Multispectral	20		
	SPOT-4/5	Panchromatic	5	60-80	11 times every 26 days
		Multispectral	10	60-80	
	Formosat-2	Multispectral	8	24	1 day
	Rapid Eye	Multispectral	6.5	77 x 1500	1 day
	ALOS	AVNIR	10	70	Several times per year as per JAXA acquisition plan
		PALSAR (Fine)	7-44	40-70	
	Radarsat-1/-2	Fine	8	50	Every few days
regional *(CR optical; CR SAR)*	**Landsat-1/2/3**	Multispectral (MSS)	80	185	Every 18 days
	Landsat-4/5	Multispectral (TM)	30	185	Every 16 days
	Landsat-7	Panchromatic (ETM+)	15	185	
		Multispectral (ETM+)	30		
	Landsat-8	Panchromatic (OLI)	15	185	Every 16 days
		Multispectral (OLI)	30		
	TerraSAR-X TanDEM-L	ScanSAR	18	100	11 day repeat cycle; 2.5 day revisit capability
	Radarsat-1/-2	Standard	25	100	Every few days
		Wide	30	150	
	ERS-2		30	100	35-day repeat cycle
	Deimos-1	Multispectral	22	600	1 day
	Terra	ASTER - VNIR	15	60	Every 16 days
		ASTER - SWIR	30	60	
		ASTER - TIR	90	60	
	SRTM	X-Band	30	220	-
	IRS-P6	LISS-3	23.5	141	5 days
national *(VCR optical; VCR SAR)*	**ALOS**	PALSAR (ScanSAR)	100	250-350	Several times per year as per JAXA acquisition plan
	Landsat-5	TM Thermal	120	185	Every 16 days
	Lansat-7*	ETM+ Thermal	120	185	Every 16 days
	Radarsat-1/-2	ScanSAR wide	100	500	Every few days
	Terra /Acqua	MODIS	250, 500, 1000	2300	At least twice daily for each satellite
	NOAA	AVHRR	1100	2399	Several times per day
	DMSP	OLS fine	560	3000	~ 12 hours
		OLS smoothed	2700	3000	
	Envisat	ASAR ScanSAR	1000	405	36-day repeat cycle

Neer (1999): VHR = very high resolution; HR = high resolution; MR = medium resolution; CR= coarse resolution; VCR = very coarse resolution

Medium-resolution remote sensing for survey planning

Over regional scales of analysis, the applicability of remote sensing datasets and methods is limited, mainly due to the affiliated geometric resolution and revisit capabilities of the particular sensor. However, due to relatively large swath width and the multispectral information contained, optical remote sensing data are widely employed for large-scale mapping of exposed land cover and usage. In conjunction with the location and extent of hazards such as landslides or floods derived from multispectral or SAR data using manual and automated techniques (Joyce et al., 2009a), these data can contribute to the post-event large-scale damage assessment in terms of a rough estimate of the affected land use (e.g., Aydöner and Maktav, 2009; Chang and Tang, 2010; Taubenböck et al., 2011a). In this manner, various sensors are suitable for the generation of large-scale and accurate land use databases. Based on these data, several authors have tried to derive indicators of regional demographic vulnerability such as regional population inventories (e.g., Aubrecht et al., 2012) or social vulnerability on the county level (e.g., Zeng et al., 2011) by the application of regionalization techniques. Furthermore, coarse resolution DEM (digital elevation model) data derived from the Shuttle Radar Topography Mission (SRTM, e.g., Farr and Kobrick, 2000) is commonly used for the coarse localization of hazard-prone regions, e.g., by the assessment of terrain elevation in case of tsunami flooding or the computation of aerial slope steepness in case of landslide events (e.g., Taubenböck et al., 2008). Relating this to vulnerability-centred applications, coarse resolution earth observation (EO) data is also frequently used for the regional assessment of hazard affected areas, above all for the determination of location and extent of hazards in the post-disaster phase.

The Landsat series of sensors (Multispectral Scanner (MSS), Thematic Mapper (TM), Enhanced Thematic Mapper (ETM+)) provide large-scale observations covering spatial extents of up to 185 km for large-scale conurbations such as megacities, as well as data continuity due to repetitive and continuous monitoring. The eighth and latest satellite from the Landsat series was launched on February 11, 2013[13]. It carries the Operational Land Imager (OLI) and the Thermal Infrared Sensor (TIRS). OLI collects data from nine spectral bands, which cover the range from visible to short wavelength infrared. The bands feature a geometric resolution of 30 m, whereas the panchromatic band allows a geometric resolution of 15 m. The TIRS instrument collects data in two long wavelength bands with a geometric resolution of 100 m to allow for thermal imaging (USGS, 2013).

In addition, these sun-synchronous sensors are a cost-effective choice as imagery is provided free of charge by the United States Geological Survey (USGS). A further distinct advantage is data comparability due to the arrangement of spectral bands within the same spectral regions. However, the sensors' relatively coarse geometric resolution presents one weakness with regards to classification due to subpixel mixed spectral information. Nevertheless, the particular datasets allow for the accurate land cover classification, especially of the distribution of urban areas in their correct dimension and form (Taubenböck et al., 2012a) as a first indicator of the spatial arrangement of human and structural exposure. Furthermore, multi-temporal imagery allows for the rough estimation of building ages and spatial urbanization rates by post-classification comparison as important vulnerability components. In addition, homogeneous urban structure types can be discriminated and characterized based on such data (Wieland et al. 2012).

[13] http://landsat.usgs.gov/landsat8.php

Meanwhile, the German radar missions TerraSAR-X and TanDEM-X have acquired two coverages of the entire landmass of the world for 2011 and 2012, which is utilized for the classification of a global urban footprint (Taubenböck et al., 2012b). Further optical and active radar sensors applied in the regional land cover mapping context are the Radarsat constellation, ERS-2[14], ASTER[15] and Envisat[16].

[14] https://earth.esa.int/web/guest/missions/esa-operational-eo-missions/ers
[15] http://asterweb.jpl.nasa.gov/
[16] http://www.esa.int/Our_Activities/Observing_the_Earth/Envisat

The Sentinel missions

A series of satellite missions that offer great promise to enhancing our capacity for vulnerability and exposure assessment are the new missions, called Sentinels, currently being developed and launched by the European Space Agency (ESA). The first of these missions, Sentinel-1A[17] (Figure 1), was launched in April, 2014 (Sentinel-1B is expected to be launched in 2016). Overall, these satellites are specifically designed to adapt to the operational needs of the Copernicus program, which is meant to provide accurate, timely and easily accessible information to improve the management of the environment, understand and mitigate the effects of climate change and to enhance civil security. Carrying a wide array of sensor systems such as radar and multi-spectral imaging instruments, these satellites will provide large-scale observations and capabilities in terms of repetitive and continuous monitoring (ESA, 2013).

The Sentinel-1 satellite system is designed to the enable continuation of C-band SAR operational applications following Europe's and Canada's series of SAR systems such as ERS-1, ERS-2, Envisat and Radarsat. With regards to the Copernicus user services and requirements, the application focus is mainly on:

(1) monitoring of sea ice zones and the arctic environment,

(2) surveillance of marine environments,

(3) monitoring of land surface motion risks,

(4) mapping of land surfaces, and

(5) mapping in support of humanitarian aid in crisis situation (ESA, 2013).

Carrying a C-band imaging radar system, Sentinel-1 is capable of acquiring data independent from weather and time of day at global coverage. Featuring two main operational modes, images will be acquired with a 5 x 20 m ground resolution and a 250 km swath width in interferometric wide swath mode and at 5 m ground resolution and a 20 km swath in wave mode (Torres et al., 2012). Sentinel-1's revisit capabilities, spatial coverage and fast-track data dissemination are key features of the mission's requirements within the framework of Copernicus. As a big enhancement compared to existing SAR systems, data will be disseminated within an hour of acquisition. The capabilities of the new system for the monitoring of land-surface motion risks are widely recognized. For example, Salvi et al. (2012) emphasized that the Sentinel-1 program will allow for an effective coverage for interferometric data over earthquake-prone regions at global level. With a revisit cycle of 12 days with one satellite, and 6 days with both, these data are considered to have the potential to substantially improve scientific knowledge and allow geodetic operational monitoring of the seismic changes. With respect to the on-going TerraSAR-X (TSX) and TanDEM-X (TDX) missions and the related "Global Urban Footprint" initiative of DLR (Esch et al., 2012), this ESA mission holds high capabilities for continuous exposure mapping or continuative urban monitoring. Taubenböck et al. (2012c) already successfully transferred and tested the originally developed classification algorithm for built-up area detection using the X-band data of TSX to the C-band of Canadian Radarsat-2 data. The transfer of the approach shows a robust classification with high accuracies.

[17] http://www.esa.int/Our_Activities/Observing_the_Earth/Copernicus/Sentinel-1

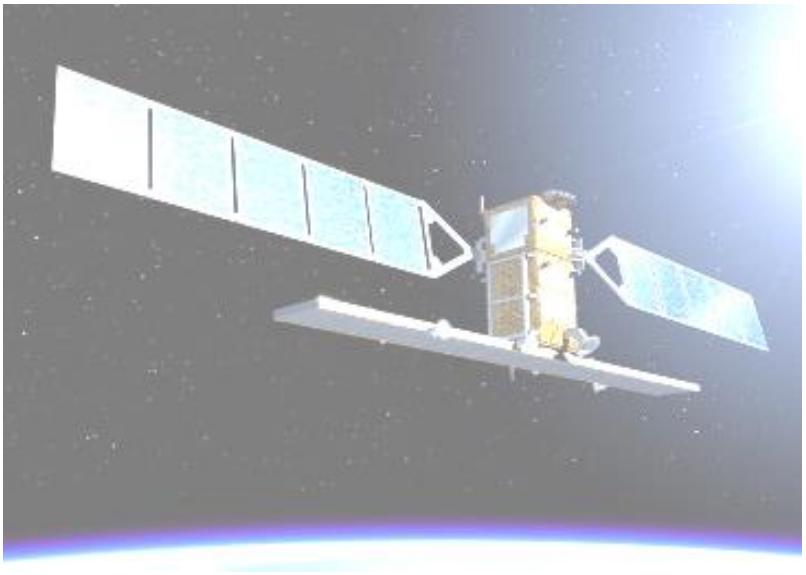

Figure 1 An artist‘s impression of a Sentinel-1 satellite (Torres et al., 2012).

Another series of satellites that will be of great value are the Sentinel-2 satellites[18] (Figure 2 **An artist’s impression of a Sentinel-2 satellite (ESA, 2013).**), with Sentinel-2A being launched in June, 2015 and Sentinel-2B’s launch planned for 2016) are designed to deliver high-resolution optical imagery at global coverage as a continuation of previous optical missions such as Landsat and Spot (Berger and Aschbacher, 2012), but with enhanced geometric and spectral capabilities. With regard to the payload specifications, the platform will carry sensors sensitive in the visible (4 bands at 10 m resolution), near infrared (6 bands at 20 m resolution) and shortwave infrared (3 band at 60 m resolution) wavelength regions, capturing imagery at a swath width of 290 km. Similarly to the Landsat series of sensors that enabled multi-temporal acquisition since the early 1970s, the superspectral system will enable consistent multi-temporal image acquisition. Orbiting at an altitude of roughly 800 km, the pair of satellites has a revisit time of five days at the equator and two to three days in mid-latitudes.

The higher spatial resolution in combination with a higher spectral resolution and a large swath enables to cover large urban areas such as mega cities at once. Thus, Sentinel-2 will provide immense potential for exposure-related remote sensing by means of land cover classification as the acquired data will allow for both the enhancement of the geometric precision of, e.g., urban footprint products, as well as an increased depth of thematic class detail by their superspectral capabilities. These improvements may allow the defining of the urbanized areas into structural types, such as classes based on built-up density or even to aim at classifying semantic structural types such as slum areas, central business districts or industrial sites. Thus, monitoring is not only to be continued, but to be thematically more detailed using the future Sentinel-2 mission. Furthermore, images of hazard events such as landslides, volcanic eruptions, and floods will be able to be acquired to determine the event‘s location and spatial extent. The capability of delivering time-critical data is therefore ensured by the very short repeat cycle of the two-satellite-constellation. Thus, Sentinel-2 imagery will provide a reliable data basis both for thematically detailed land-cover classifications and the derivation of frequent land-change detection products. In essence, Sentinel-2 will combine a large swath, frequent revisit, and systematic acquisition of all

[18] http://www.esa.int/Our_Activities/Observing_the_Earth/Copernicus/Sentinel-2/Introducing_Sentinel-2

land surfaces at high-spatial resolution and with a large number of spectral bands, surpassing the overall capabilities of past missions (ESA, 2013).

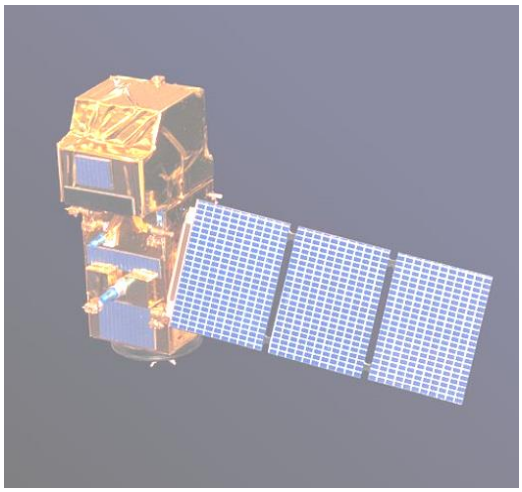

Figure 2 An artist's impression of a Sentinel-2 satellite (ESA, 2013).

The SATEX QGIS plugin

Purpose of the SATEX plugin

The SATEX plugin that provides two algorithms for the processing of one or multiple Landsat scenes within a region of interest towards a Landuse/Landcoverage classification streamlining all required processing steps to perform a libsvm/orfeo toolbox (OTB) pixel based classification.

Installation

The SATEX software package can be downloaded from the GFZ github repository[19] and installed via the QGIS Plugin Manager or by putting the cloned repository in *qgis2/python/plugins/* and running the '*make deploy*' script from within the repository.

Software requirements

The plugin requires an installation of the Orfeo Toolbox[20] (OTB). On Windows it is possible to install it via OSGeo4W[21], on Linux it can be installed from the packages related to the specific operating distribution, or can be compiled from source, using the source code available from its git repository[22].

Note: Some Linux distributions split OTB into different packages. Therefore, in order for this plugin to work, the user is requested to make sure that the python wrappers are installed alongside with the OTB library. This can be checked by opening the Python Console and executing:

- *import otbApplication*
- otbApplication.Registry.GetAvailableApplications()

This should return a non-null list of available otb functions.

Structure of the Plugin

The Plugin is structured into two modules:

1. Preprocessing
2. Classification

[19] https://github.com/GFZ-Centre-for-Early-Warning/REM_satex_plugin
[20] www.orfeo-toolbox.org
[21] http://trac.osgeo.org/osgeo4w/
[22] https://github.com/orfeotoolbox/OTB

In the **Preprocessing** module, Landsat scenes[23] are:

1) cropped to the region of interest, which is provided as, e.g., a polygon feature in a vector file,
2) the separate spectral Bands are stacked,
3) a virtual raster tile is created out of these, i.e., in case the region of interest stretches over more than one Landsat scene, these are virtually mosaiced.

If present, the panchromatic band 8 (Landsat 7 and 8) is excluded from the layers. The **Classification** algorithm performs a classification of a raster file, such as the one, e.g., resulting from the **Preprocessing** algorithm. The classification is done either by using a provided trained Support Vector Model (SVM) from the OTB, or training and testing a SVM on-the-fly using a provided ground truth testing/training data set. In the case where on-the-fly training/testing is performed, the provided ground truth data is randomly split into testing (~20%) and training (~80%) parts, the latter being used in the libsvm implementation of OTB to create a SVM. This SVM (or the external SVM) is then used to classify the image. The resulting raster file with class labels is then tested with the testing dataset (or all features of the provided vector layer in the case where an external SVM model was provided) and a confusion matrix (a matrix which should have zero values outside the diagonal, any other values means there is a miss-classification) is produced. Finally, the resulting raster file is sieved, i.e., regions consisting of few pixels are merged to the surrounding.

Instructions on SATEX plugin´s usage

Preparation of the necessary data (outside the plugin):

1. Create a vector layer with a feature containing your region of interest (ROI) as a polygon and save it in ESRI shapefile format[24]. We will refer to this file as the **ROI vector**. An example ROI is presented in Figure 1.

2. Download the Landsat scene(s) from http://earthexplorer.usgs.gov/ (you will need an account - free of cost) covering your region of interest. An example of a full Landsat image is displayed in Figure 3, and a close-up of the ROI is shown in Figure 4.

[23] Such images need to be located in a directory, such as, e.g., the directory created when extracting from the downloaded zip archive of a Landsat 8 scene as can be found on EarthExplorer http://earthexplorer.usgs.gov/.
[24] https://www.esri.com/library/whitepapers/pdfs/shapefile.pdf

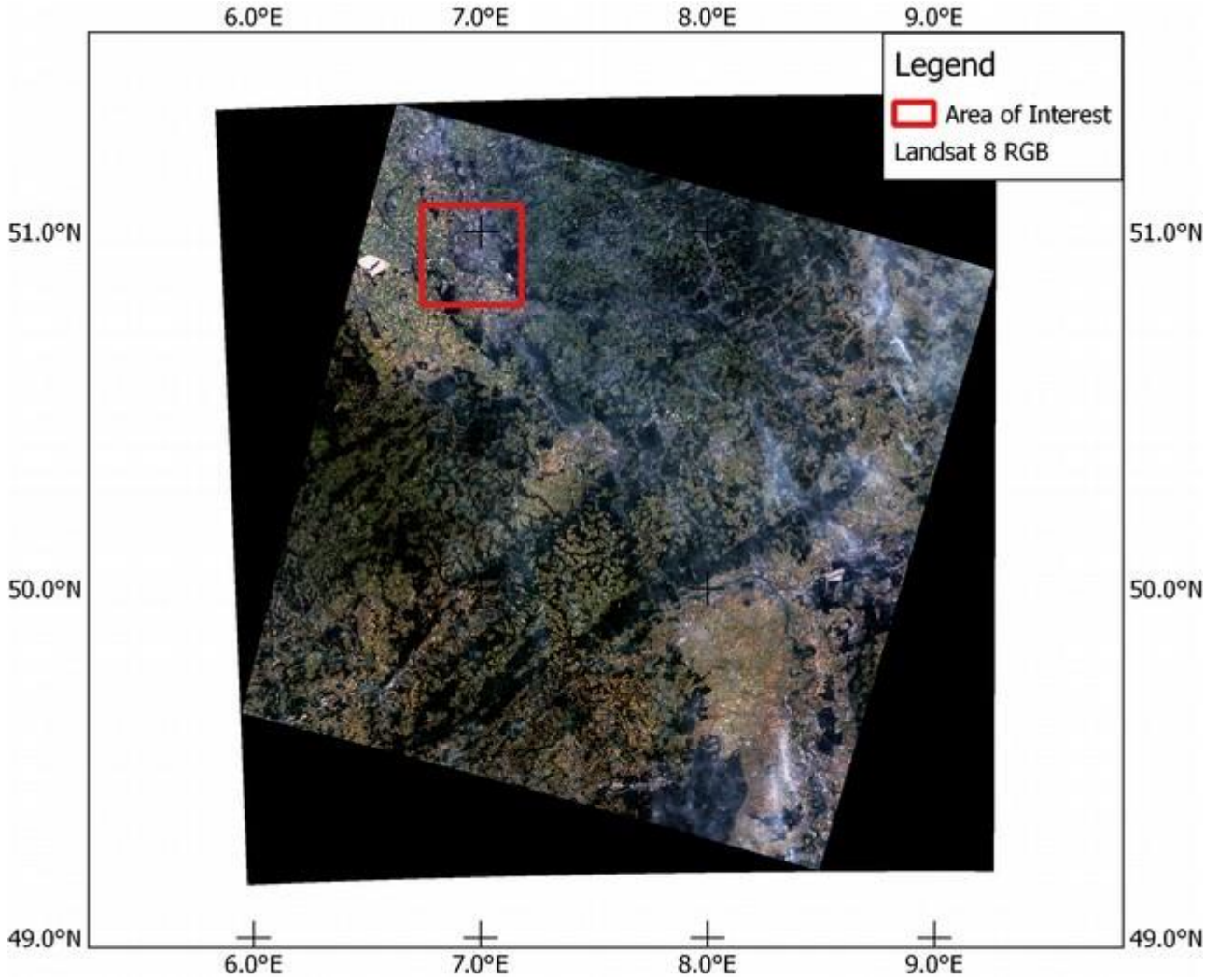

Figure 3 An example of a full Landsat 8 image. This image covers an area of approximately 10'000 squared km. The considered Region of Interest (ROI) is depicted by the red square in the upper left corner.

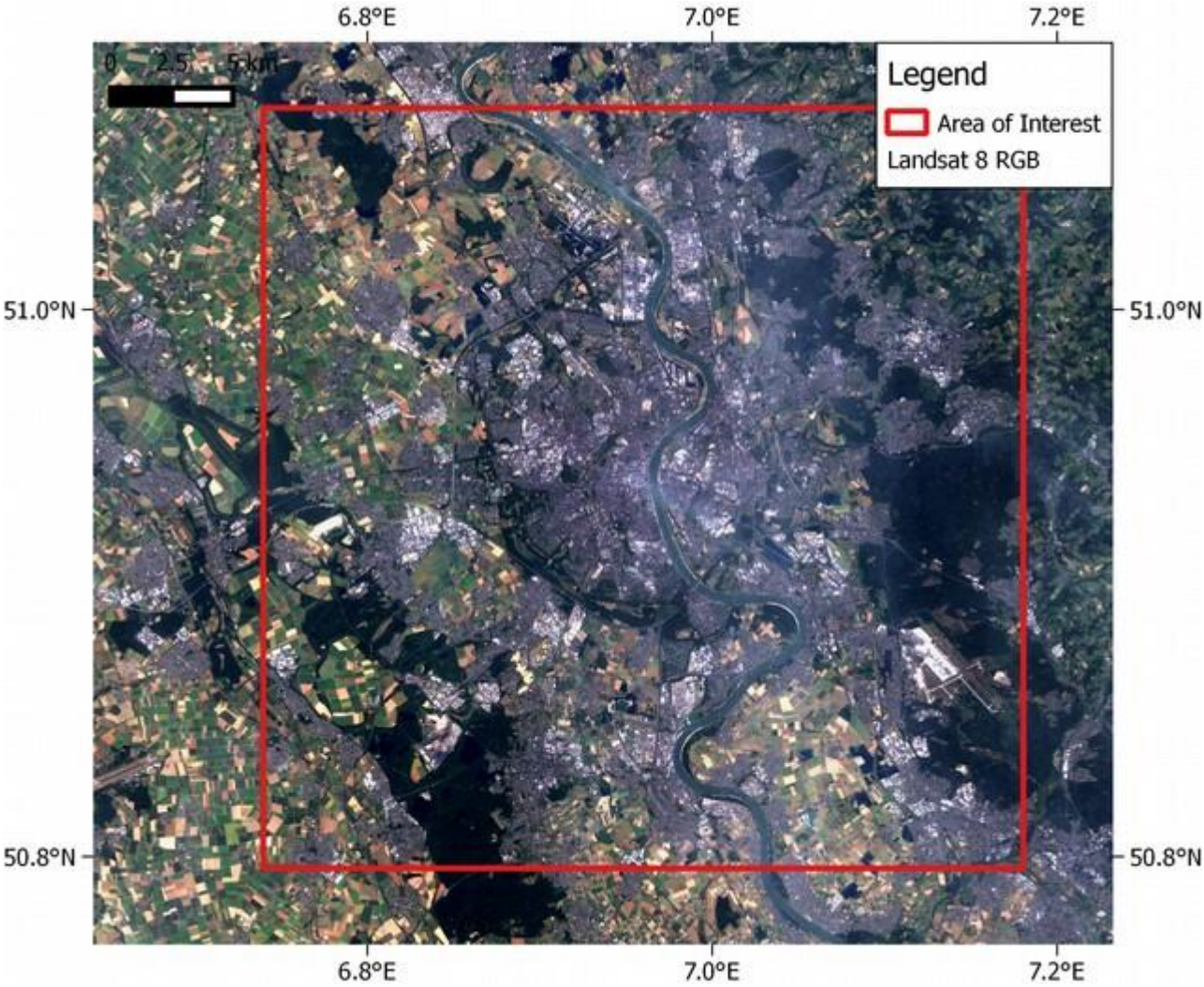

Figure 4 Landsat image (Figure 3) zoomed to the selected ROI. The region contains the city of Cologne, Germany, one of the SIBYL test cases.

3. Extract the downloaded archive of the scene. Note: In case you use several scenes for your region of interest, merge the resulting directories into one, i.e., all **.TIF* files corresponding to the different bands of the scenes have to be in a single directory. This will be referred to as the **Band directory.**

4. Create a vector layer containing ground truth data in the form of polygons with an attribute containing the labels of your desired classes within your region of interest. We will refer to this as the **Train/Test vector**.

In order to create the Train/Test dataset, it is necessary to rely on previous in-situ information, local knowledge or available global high-resolution imagery, such as that provided by GOOGLE(TM) (e.g., Figure 5). This type of imagery is not suitable for automated processing, both for technical and legal reasons, but can be easily exploited to gather quality information on the different types of Land Use / Land Cover in the considered geographical area.

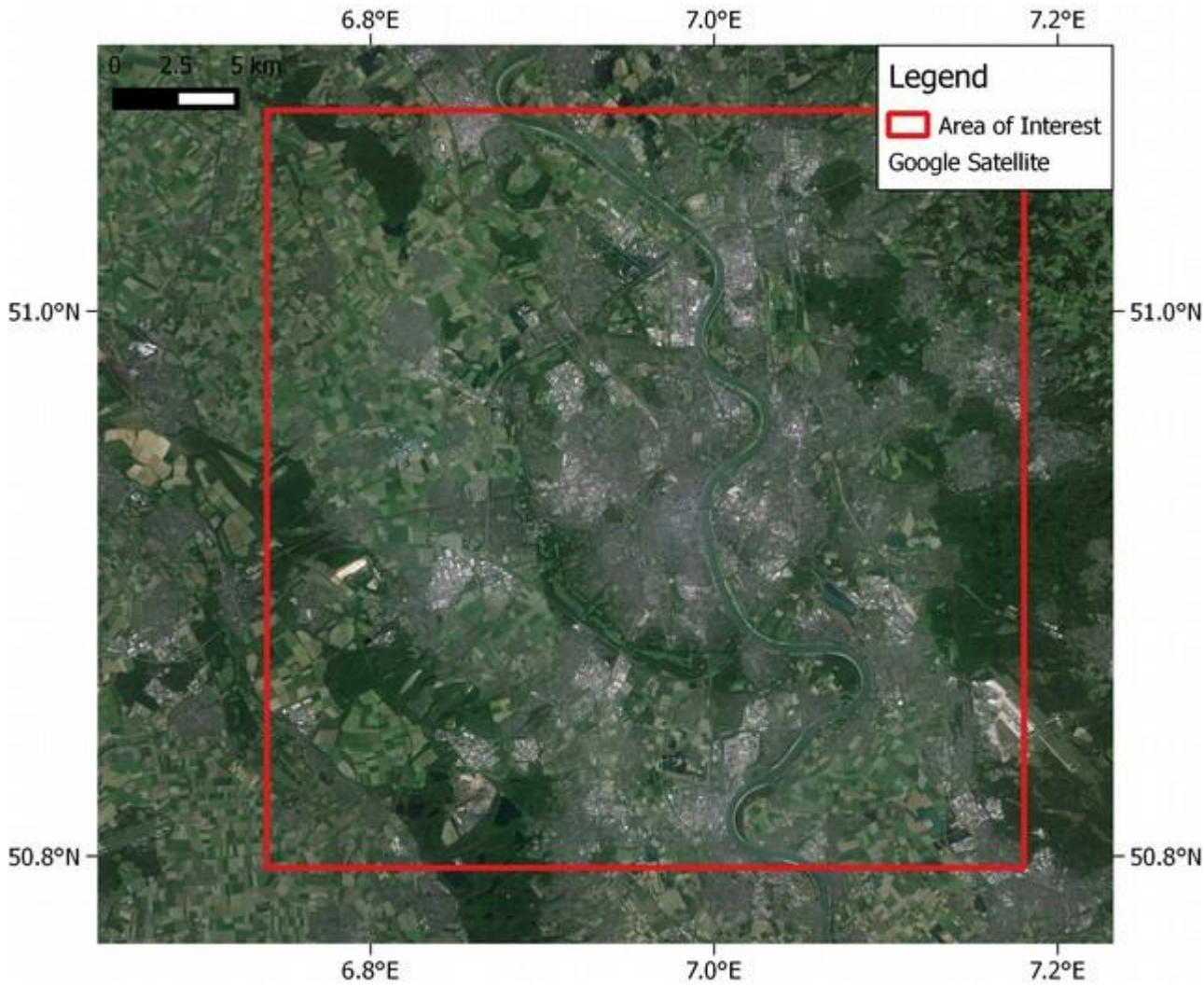

Figure 5 Example of a high resolution image of the selected ROI (source: Google Map).

The resulting Training / Testing dataset is depicted in Figure 6. Examples of the LULC pattern used to train the system are shown in the Figure 7 to Figure 13. In particular, Figure 13 shows an example of the RES! Class (residential, high density). In Figure 14, the same area is displayed in the Landsat image. This is the actual data fed into the learning machine. Let us remark that, even if given the low geometrical resolution, the Landsat image seems to our eyes not very informative, most of the actual informational content resides in the multiple spectral bands. These bands are able to capture a rich spectrum of wavelengths strongly associated to different materials (and therefore, different interactions with the electromagnetic radiation). This information content is barely visible, because the human eye can only see colours ranging from Blue to Red. Such information cannot be easily mapped into a colour image, but is efficiently exploited by the Support Vector Machine in order to clearly separate the different proposed classes.

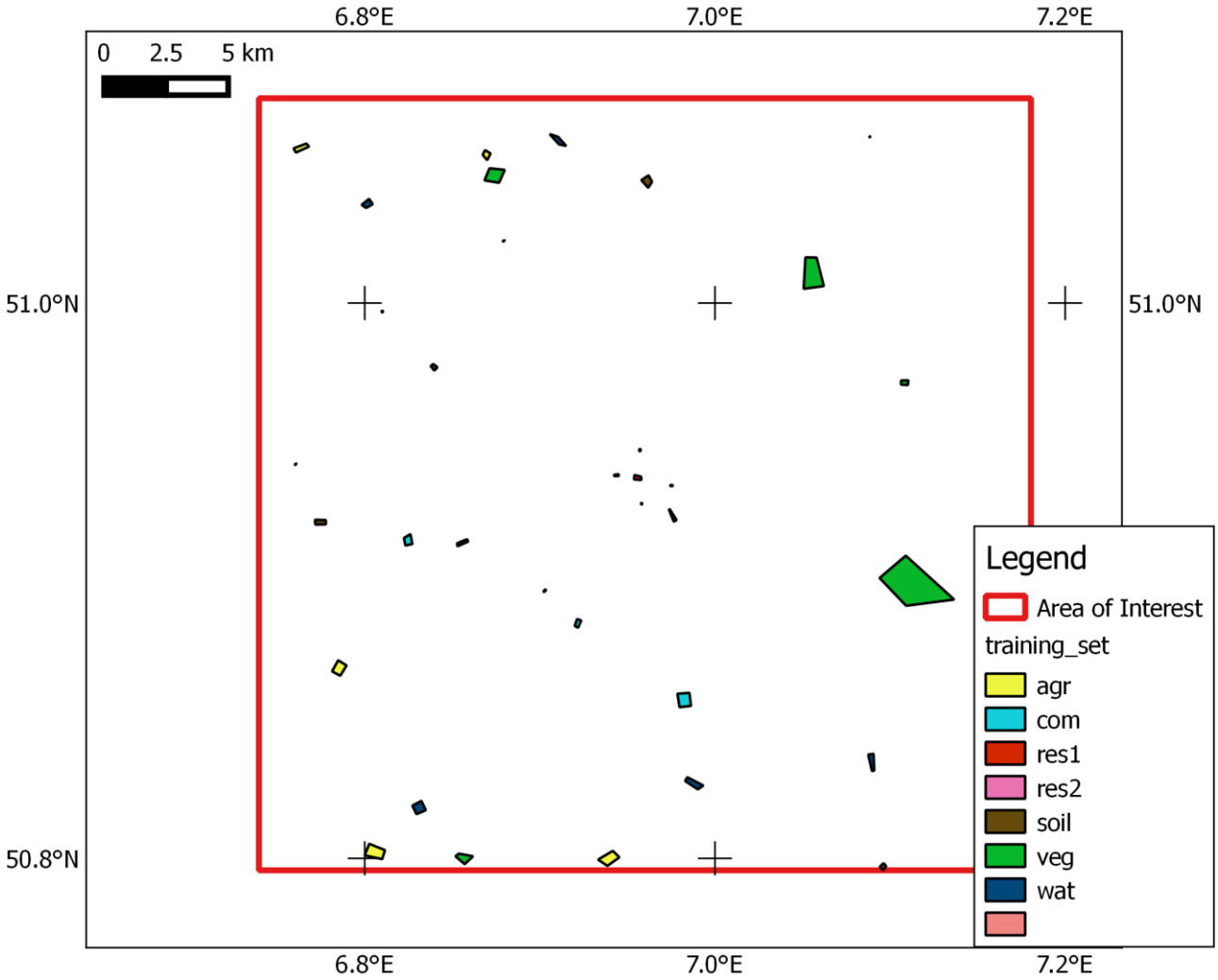

Figure 6 Arrangement of the training data, in terms of several labelled polygons, within the considered ROI (see Figure 3 and Figure 4).

Figure 7 Example of the AGR (agricultural) label in a High Resolution image.

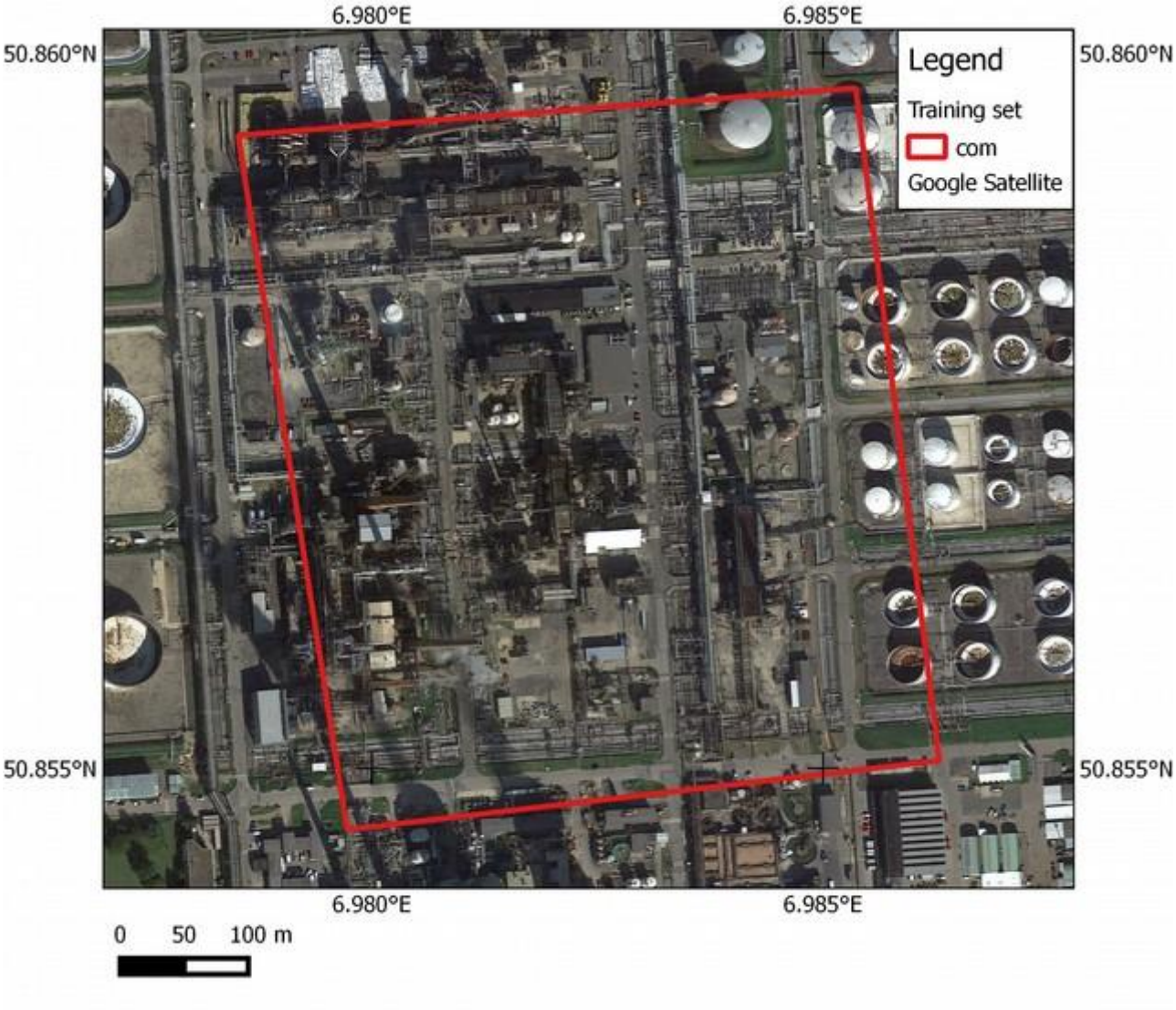

Figure 8 Example of the COM (Commercial, Industrial) label in a High Resolution image.

Figure 9 Example of the RES2 (Residential, low density) class in a High Resolution image.

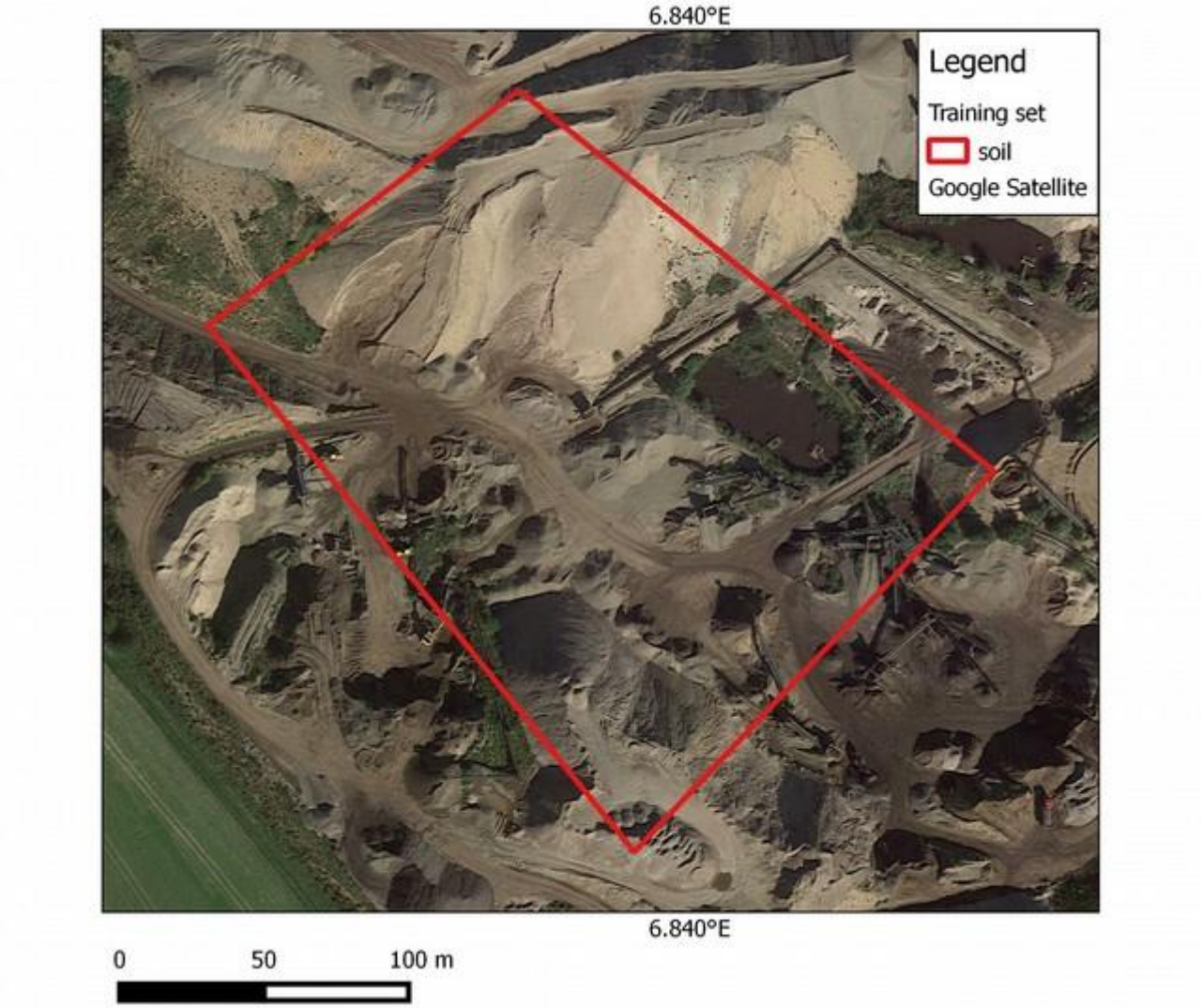

Figure 10 Example of the SOIL (unsealed road, soil) class in a High Resolution image.

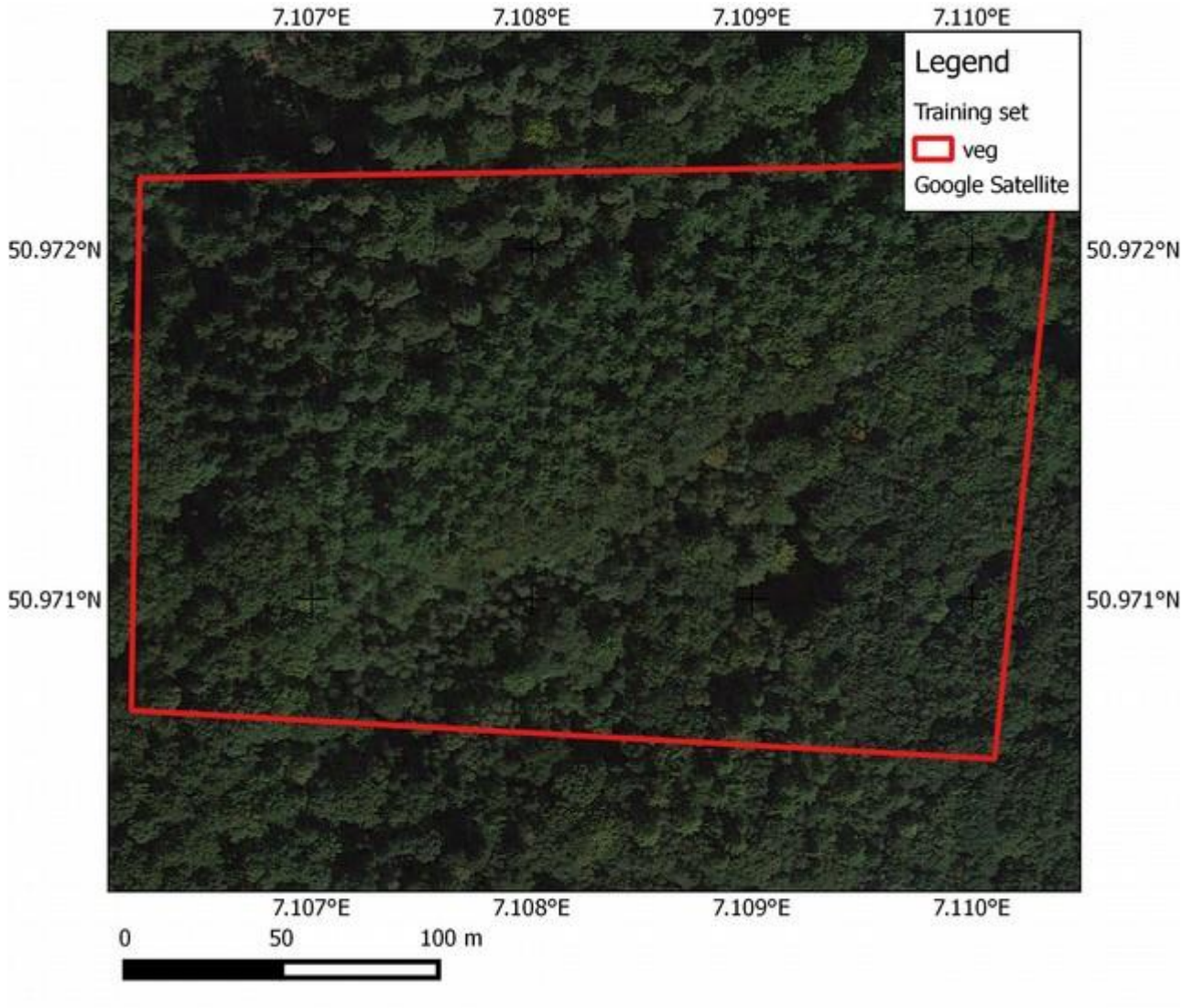

Figure 11 Example of the VEG (vegetation) class in a High Resolution image.

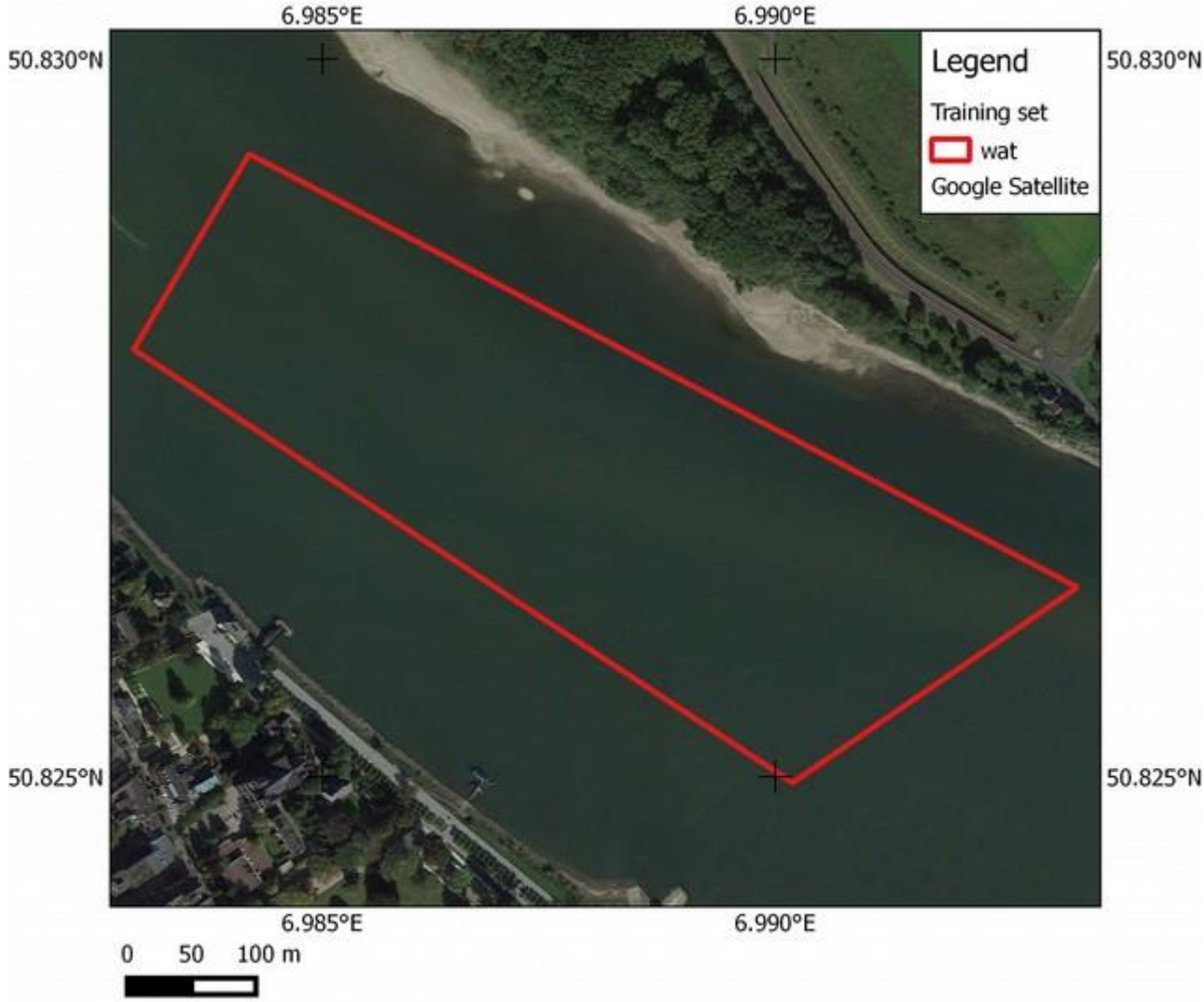

Figure 12 Example of WAT (water) class in a High Resolution image.

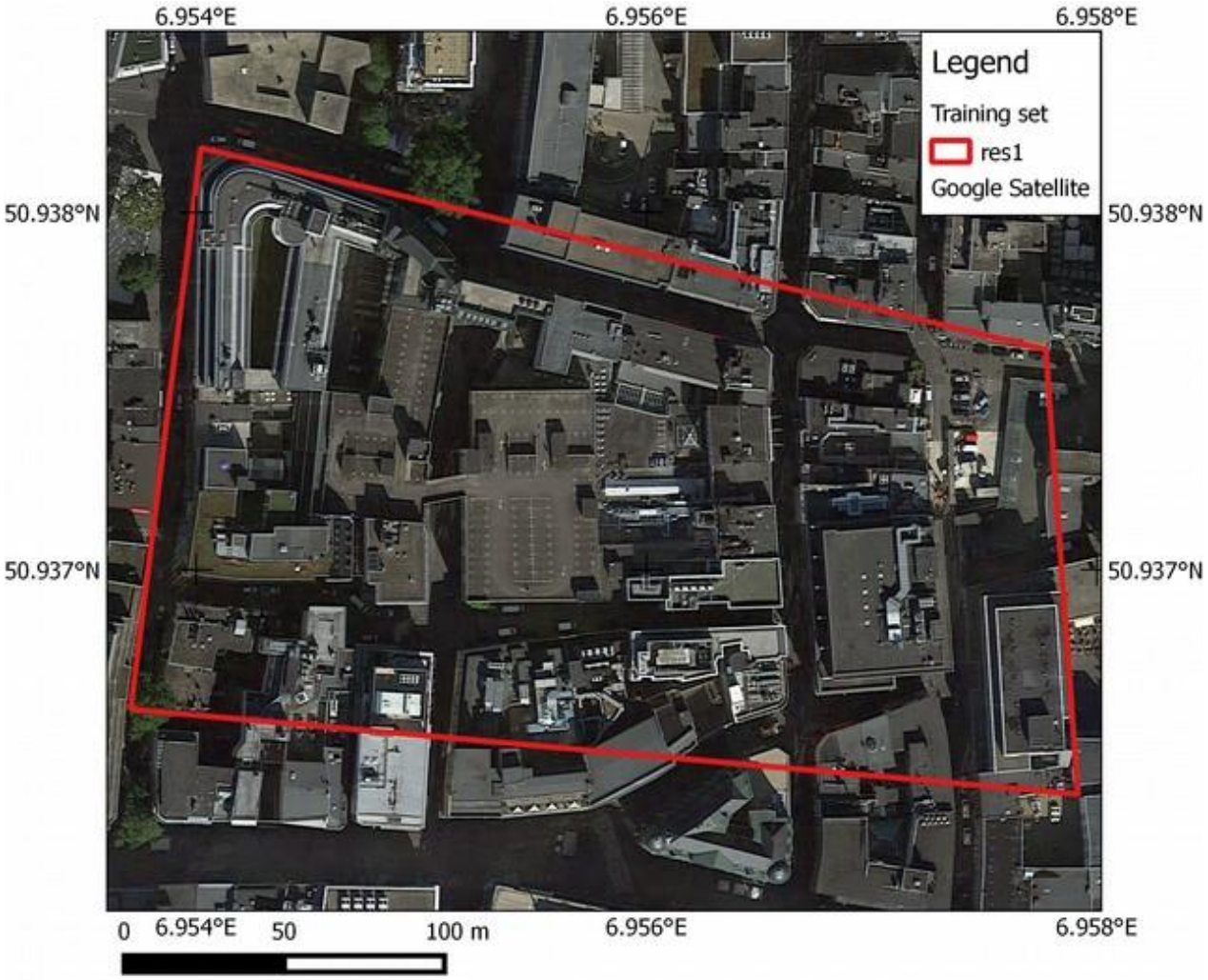

Figure 13 Example of RES1 (Residential, high density) class in a High Resolution image.

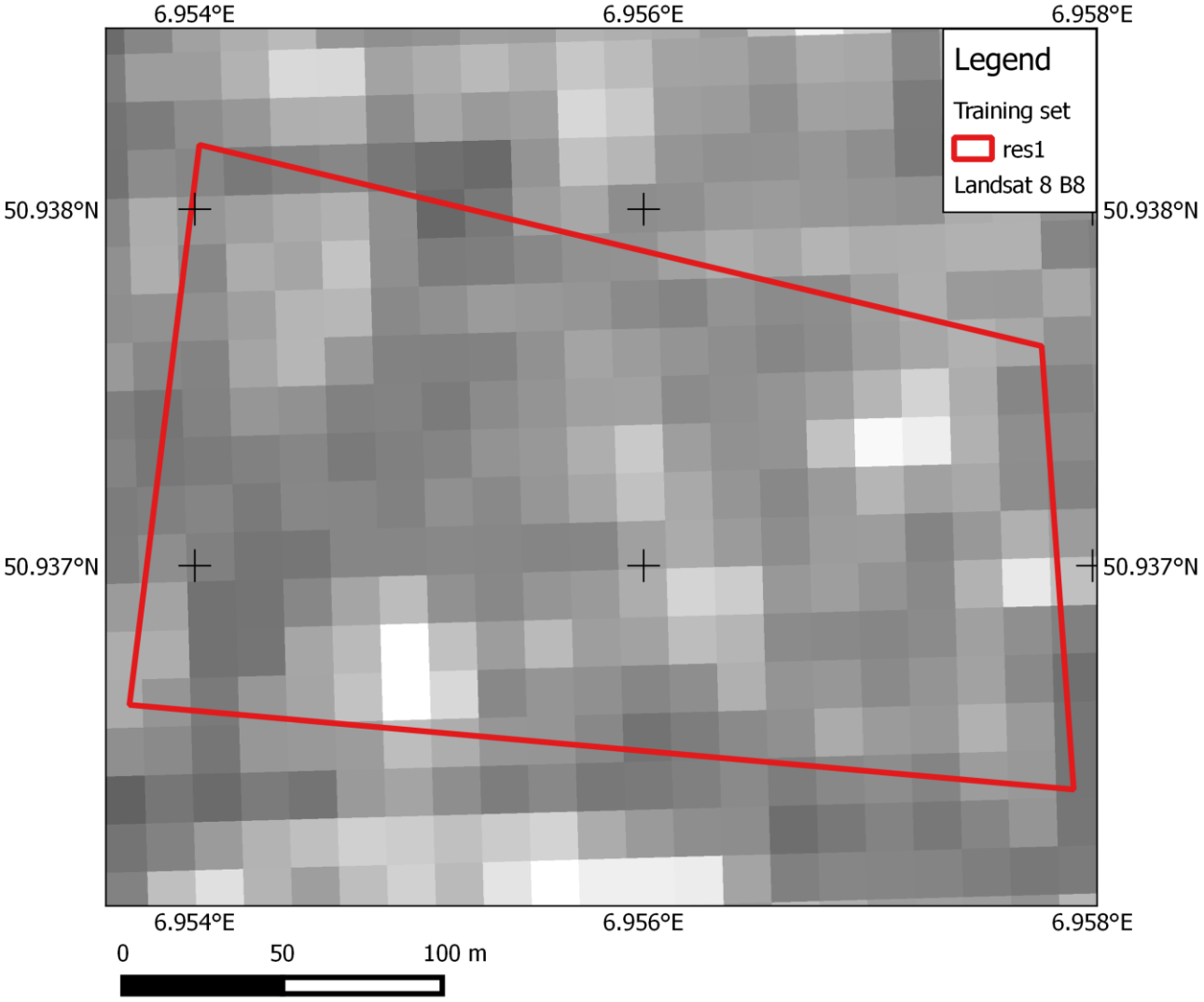

Figure 14 Example of RES1 (Residential, high density, Figure 13) class as seen in a Landsat 8 image, considering the panchromatic band only (resolution 15m).

Preprocessing

What to enter?

The module interface is shown in Figure 15. It has three white text fields which can be edited. In the first text field *Directory Landsat bands* the path to the **Band directory** must be specified (see section **Preparation of the necessary data**), alternatively you can use the button with the three dots next to the text field to open a file browser to search for the file. In the second textfield *Input ROI (shp)* you have to provide the location of the **ROI vector** (see section **Preparation of the necessary data**). In the last text field *Output (vrt)* you can specify the location and filename of the virtual raster tile the module will produce. If you tick the checkbox *Add result to canvas* the resulting output will be added to your QGIS layers. Finally, run the module by clicking the *OK* Button. Close the dialog without running it via the *Close* Button.

Note: Depending on the machine being used and the size of the ROI, the processing might take some time and during that time QGIS might be non-responsive.

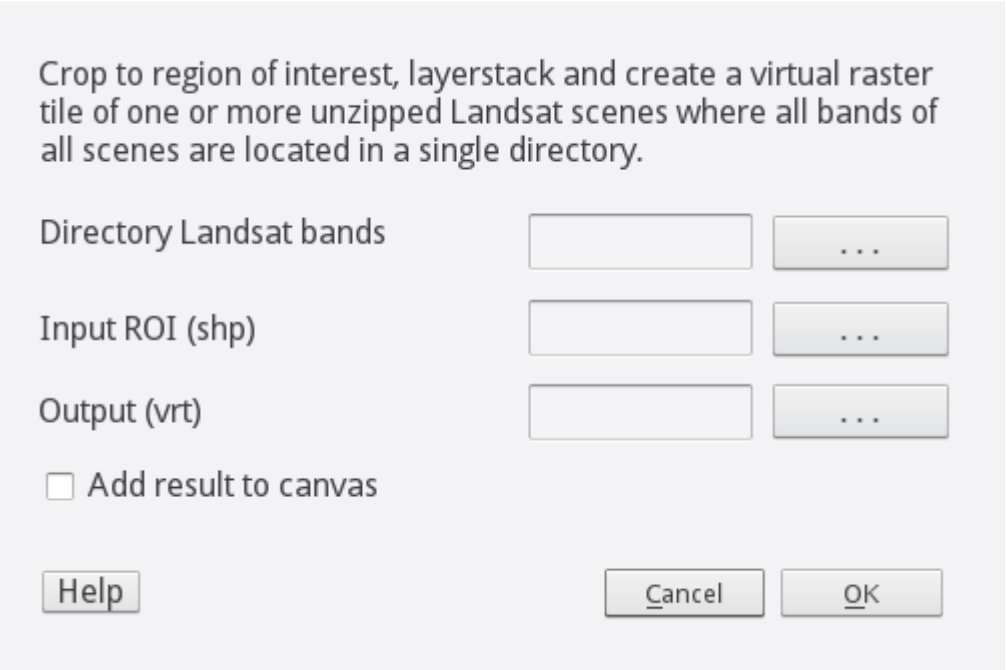

Figure 15 Preprocessing dialog in the QGIS plugin.

What happens?

The module will first check the number of different scenes that are present in the **Band directory** and then crop each band for each scene to the region of interest as specified by the **ROI vector** (checking that they at least partly overlap) and stack the bands into a single file for each of the scenes. These files are created in the same directory as you specified for the output virtual raster

tile *Output (vrt)* with a file suffix like *_satex_mul.TIF*. Finally, they are virtually stitched together in the file that is specified in the text field **Output (vrt)**.

Note: The resulting **.vrt* file only links the *_satex_mul.TIF* files created in the **Band directory** and does not contain the actual data! If you need to transfer the file save it as a regular **.TIF* file.

Classification

In the classification phase, the datasets and raster images described in the preceding sections are integrated to generate a suitable segmentation of the considered area.

What to enter?

The interface for the module is shown in Figure 16. It has four white text fields which can be edited. In the first text field *Input raster (*.TIF or .vrt)* the location of the file to be classified has to be defined (e.g., the virtual raster tile resulting from the **Preprocessing** module). Alternatively one can use the button with the three dots next to the text field to open a file browser to search for the file. In the second textfield *Training/Testing vector (*.shp)* one must provide the location of the **Training/Testing vector** (see section **Preparation of the necessary data**). In the third text field *Class label column name* you have to specify the name of the column in your **Training/Testing vector** that holds the labels of your classes. If there is already an OTB Support Vector model from, e.g., another region, and one wishes to use this for the classification rather than training a new one, you can tick *Provide external SVM* and specify the location of this model in the text field *External SVM Model*. In the text field **Output (*.TIF)**.

The location and file name of the resulting raster file containing the class labels has to be specified. In case one wishes to remove small classification regions, e.g., if a region is consisting of only 4 pixels and one wishes to merge these with the largest neighbouring regions, tick the option *Sieve result for regions with pixels less than* and specify the minimum number of pixels to remain in the output in the text field next to it. If the checkbox *Add result to canvas* is ticked, the resulting output will be added to your QGIS layers.

Figure 16 Classification dialog in the QGIS plugin.

What happens?

The module distinguishes two cases. If an external SVM model is provided, the image is classified using this model and all provided features in the **Training/Testing vector** are used for testing (making sure that all features are covered by the raster file). A csv file containing the Confusion Matrix is created in the same location as the **Training/Testing vector** with the same name, but ending with **_CM.csv* instead of **.shp*. In the second case where no external SVM model is provided, the **Training/Testing vector** will be split into two files at the same location as the **Training/Testing vector** and with the same name, but ending with **_test.shp* and **_train.shp*, respectively. The splitting is done with the fixed ratio (discussed above) of features of ~80% training and ~20% testing data with the same number of feature samples (at least one) from each class. (**Note:** The number of pixels in each of the sets depends on the size of the features and is not controlled). The features of the **_train.shp* file are then used to train a SVM based on the libsvm implementation of OTB. The resulting model is created at the location of the **Training/Testing vector** and with the same name, but ending with **_svmModel.svm* is then used to classify the *Input raster*. The features of the **_test.shp* file are then used to calculate a

Confusion Matrix at the same location as the **Training/Testing vector** and the same name, but ending with **_CM.csv* instead of **.shp*.

The resulting labelling of the Landsat image portion corresponding to the ROI is shown in Figure 17. It is possible to observe that, even with a very small number of samples available for training and testing, the SATEX plugin provides a first-order classification which allows for the better understanding of the patterns of an urban area, as defined by the interleaved classes. The resulting dataset can moreover be used to plan a suitable in-situ survey where additional, more detailed data will be collected.

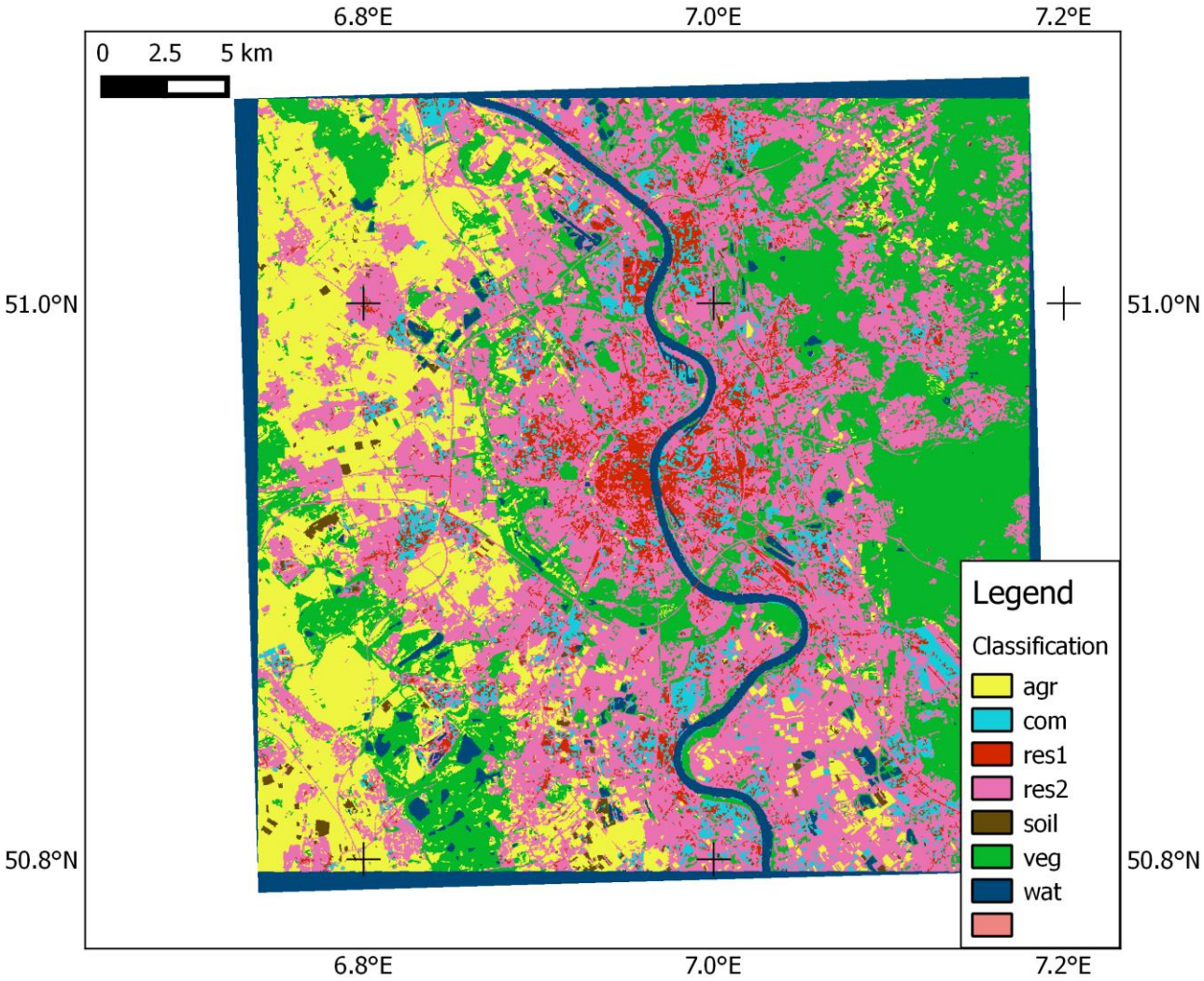

Figure 17 Resulting pixel-based classification of the input Landsat image in correspondence of the selected ROI. The pixels are coloured according to the specific class estimated by the statistical learning machine.

Software License

References and suggested reading

Aubrecht, C., Özceylan, D., Steinnocher, K. and Freire, S. (2012) Multi-level geospatial modeling of human exposure patterns and vulnerability indicators. Natural Hazards, 68(1), 147-163.

Aydöner, C., Maktav, D. (2009) The role of the integration of remote sensing and GIS in land use/land cover analysis after an earthquake. International Journal of Remote Sensing, 30, 1697–1717.

Berger, M., Aschbacher, J. (2012) Preface: the sentinel missions-new opportunities for science. Remote Sensing of Environment, 120, 1-2.

Birkmann, J. (2006) Indicators and criteria for measuring vulnerability: theoretical bases and requirements. In: Birkmann, J. (ed.) Measuring vulnerability to natural hazards. United Nations University Press, New York, 55–77.

Borfecchia, F., Pollino, M., De Cecco, L., Lugari, A., Martini, S., La Porta, L., Ristoratore, E. and Pascale C (2010) Active and passive remote sensing for supporting the evaluation of the urban seismic vulnerability. Italian Journal of Remote Sensing, 42,129–141.

Borzi, B., Dell'Acqua, F., Faravelli, M., Gamba, P., Lisini, G., Onida, M. and Polli, D. (2011) Vulnerability study on a large industrial area using satellite remotely sensed images. Bulletin of Earthquake Engineering, 9, 675–690.

Brunner, D., Lemoine, G. and Bruzzone, L. (2010) Earthquake damage assessment of buildings using VHR optical and SAR imagery. IEEE Transactions on Geoscience and Remote Sensing, 48, 2403–2420.

Cartwright, S. (2005) National Civil Defence Emergency Management Plan Order 2005. Published under the authority of the New Zealand Government, Wellington, New Zealand, 68 pp.

CEOS (2012) CEOS mission, instruments and measurements database online. Available at http://database.eohandbook.com/ Accessed 23 Jun 2013

Chang, L. and Tang, Z. (2010) Using remote sensing technology to assess land—use changes after the Northridge Earthquake. Disaster Advances, 3, 5–10.

Chen, K. (2002) An approach to linking remotely sensed data and areal census data. International Journal of Remote Sensing, 23, 37–48.

Chiroiu, L., Adams, B. and Saito, K. (2006) Advanced techniques in modeling, response and recovery. In: Oliveira, C.S., Roca, A., Goula, X. (eds.) Assessing and managing earthquake risk. Springer, Dordrecht, 427–448.

CSA (2012) Canadian space agency—RADARSAT Mission description. Available at http://www.asc-csa.gc.ca/eng/satellites/radarsat/description.asp Accessed 11 Jun 2013

Cunningham, D., Grebby, S., Tansey, K., Gosar, A. and Kastelic, V. (2006) Application of airborne LiDAR to mapping seismogenic faults in forested mountainous terrain, southeast Alps, Slovenia. Geophysical Research Letters, 33, L20308.

Dech, S. (1997) Anwendung der Satellitenfernerkundung. Von der geowissenschaftlichen Forschung zum operationellem Einsatz. DLR Forschungsbericht, 97, 52.

Defourny, P., Schouten, L., Bartalev, S., Bontemps, S., Caccetta, P., de Witt, A., di Bella, C., Gerard, B., Giri, C., Gond, V., Hazeu, G., Heinimann, A., Herold, M., Jaffrain, G., Latifovic, R., Ling, H., Mayaux, P., Muncher, S., Nonguierma, A., Stibig, H-J., Van Bogaert, E., Vancutsem, C., Bicheron, P., Leroy, M. and Arino, O. (2009) Accuracy Assessment of a 300-m Global Land Cover Map: the GlobCover Experience. Proceedings of the 33rd International Symposium on Remote Sensing of Environment (ISRSE), Stresa, Italy, May 2009.

Deichmann, U., Ehrlich, D., Small, C. and Zeug, G. (2011) Using high resolution satellite data for the identification of urban natural disaster risk. Global Facility for Disaster Reduction and Recovery, Washington, DC.

Dell'Acqua, F., Lisini, G. and Gamba, P. (2009) Experiences in optical and SAR imagery analysis for damage assessment in the Wuhan, May 2008 Earthquake. IEEE International Geoscience and Remote Sensing Symposium, 1–5, 2417–2420.

DESDynI (2011) Deformation, ecosystem structure and dynamics of ice—mission concept. Available at http://desdyni.jpl.nasa.gov/mission/. Accessed 11 Jun 2013

DigitalGlobe (2012) WorldView-3. Available at http://www.digitalglobe.com/downloads/WorldView3-DSWV3-Web.pdf Accessed 11 Jun 2013.

Ding, X. and Huang, W. (2011) D-InSAR monitoring of crustal deformation in the eastern segment of the Altyn Tagh Fault. International Journal of Remote Sensing, 32,1797–1806.

DLR (2010) TanDEM-X Science Home – Mission goal. Available at http://www.dlr.de/hr/en/desktopdefault.aspx/tabid-2317/3669_read-5492/ Accessed: 26 Jun 2013

DLR (2011) Corine Land Cover – Germany. Available at http://www.corine.dfd.dlr.de/intro_en.html Accessed 14 Jun 2013

DLR (2012) EnMap – Germany's hyperspectral satellite for Earth Observation. Available at http://www.dlr.de/dlr/en/desktopdefault.aspx/tabid-10379/567_read-421/#gallery/2671 Accessed 11 Jun 2013 Accessed 14 Jun 2013

DLR (2013) DLR-ZKI successful activities within the GMES emergency responser service. Available at http://www.zki.dlr.de/de/gmes-ers Accessed 11 Jun 2013

Dobson J.E., Bright, E.A., Coleman, P.R., Durfee, R.C. and Worley, B.A. (2000) LandScan: a global population database for estimating populations at risk. Photogrammetric Engineering and Remote Sensing, 66, 849–857.

Ebert, A., Kerle, N. and Stein, A. (2009) Urban social vulnerability assessment with physical proxies and spatial metrics derived from air- and spaceborne imagery and GIS data. Natural Hazards, 48, 275–294.

EC (2012) Mapping Guide – for a European Urban Atlas. Available at ec.europa.eu/regional_policy/tender/pdf/2012066/annexe2.pdf Accessed 14 Jun 2013.

EEA (2006) Corine land cover database passes accuracy test. Available at: http://www.eea.europa.eu/highlights/Ann1151398593 Accessed 14 Jun 2013

Ehrlich, D., Zeug. G., Gallego, J., Gerhardinger, A., Caravaggi, I. and Pesaresi, M. (2010) Quantifying the building stock from optical high-resolution satellite imagery for assessing disaster risk. Geocarto International, 25(4), 281–293.

Eicher, C.L. and Brewer, C.A. (2001) Dasymetric mapping and areal interpretation interpolation: implementation and evaluation. Cartography and Geographic Information Science, 28, 125-138.

Eineder, M., Friedrich, A., Minet, C., Bamler, R., Flerit, F. and Hajnsek, I. (2009) Scientific requirements and feasibility on an L-band mission dedicated to measure surface deformation. IEEE International Geoscience and Remote Sensing Symposium. 12–17 July 2009, Cape Town, South Africa.

eoPortal (2013) Satellite Missions Database. Available at: https://directory.eoportal.org/web/eoportal/satellite-missions Accessed 11 Jun 2013

ESA (2011) GlobCover. Available at: http://due.esrin.esa.int/globcover/ Accessed 14 Jun 2013

ESA (2012) Deimos-1. Available at: at: https://earth.esa.int/web/guest/missions/3rd-party-missions/current-missions/deimos-1 23 Jun 2013

ESA (2013) European Space Agency – ESA's Sentinel satellites: Overview, Sentinel-1, Sentinel-2. Available at http://www.esa.int/Our_Activities/Observing_the_Earth/GMES/Sentinel-1 Accessed 11 Jun 2013 Accessed 11 Jun 2013

Esch, T., Dech, S., Roth, A., Schmidt, M., Taubenböck, H., Heldens, W., Thiel, M., Wurm, M. and Klein, D. (2009) Monitoring and assessment of urban environments using space-borne earth observation data. In: Kreck, A., Rumor, M., Zlatanova, S., Fendel, E. (eds) Urban and regional data management. Taylor & Francis Group, London, 385–398.

Esch, T., Taubenböck, H., Roth, A., Heldens, W., Felbier, A., Thiel, M., Schmidt, M., Müller, M., Müller, A. and Dech, S. (2012) TanDEM-X mission—new perspectives for the inventory and monitoring of global settlement patterns. Journal of Applied Remote Sensing, 6, 061702.

Farr, T.G. and Kobrick, M. (2000) Shuttle Radar Topography Mission produces a wealth of data, EOS Transactions, 81, 583-585.

Fielding, E.J., Wright, T.J., Muller, J., Parsons, B.E. and Walker, R. (2004) Aseismic deformation of a fold-and-thrust belt imaged by synthetic aperture radar interferometry near Shahdad, southeast Iran. Geology, 32, 577–580.

French S.P. and Muthukumar, S. (2006) Advanced technologies for earthquake risk inventories. Journal of Earthquake Engineering, 10, 207–236.

Fu, B., Ninomiya, Y., Lei, X., Toda, S. and Awata, Y. (2004) Mapping active fault associated with the 2003 Mw 6.6 Bam (SE Iran) earthquake with ASTER 3D images. Remote Sensing of Environment, 92, 153–157.

Gamba, P. and Houshmand, B., (2002) Joint analysis of SAR, LIDARand aerial imagery for simultaneous extraction of land cover, DTM and 3D shape of buildings. International Journal of Remote Sensing, 23, 4439– 4450.

Ge, Y., Xu, J., Liu, Q., Yao, Y. and Wang, R. (2009) Image interpretation and statistical analysis of vegetation damage caused by the Wenchuan earthquake and related secondary disasters. Journal of Applied Remote Sensing, 3:031660.doi:10.1117/1.3141726 (26 May 2009).

Geiß, C. and Taubenböck, H. (2013) Remote sensing contributing to assess earthquake risk: from a literature review towards a roadmap. Natural Hazards, 68(1), 7-42, doi: 10.1007/s11069-012-0322-2.

Geiß, C., Taubenböck, H., Wurm, M., Esch, T., Nast, M., Schillings, C. and Blaschke, T. (2011) Remote Sensing-Based Characterization of Settlement Structures for Assessing Local Potential of District Heat. Remote Sensing 3, 1447–1471.

Geiß, C., Wurm, M., Taubenböck, H., Heldens, W. and Esch, T. (2011) Comparison of selected impervious surface products derived from remote sensing data. In: Proceedings of the JURSE 2011. Presented at the JURSE 2011, Munich.

GFZ (2012) EnMAP – Environmental Mapping and Analysis Program. Available at http://www.gfz-potsdam.de/portal/gfz/Struktur/Departments/Department+1/sec14/projects/enmap;jsessionid=8109B074FB80292C62335A5838A069EA Accessed 12 Jun

G-MOSAIC (2012) G-MOSAIC: GMES pilot services for security. Available at http://www.gmesgmosaic.eu/. Accessed 14 Jun 2013

Guo, H. (2010) Understanding global natural disasters and the role of earth observation. International Journal of Digital Earth, 3, 221–230.

Heldens, W., Heiden, U., Esch, T., Stein, E. and Müller, A. (2011) Can the future EnMAP mission contribute to urban applications? A Literature Survey. Remote Sensing, 3, 1817–1846.

Hong, Y., Adler, R. and Huffmann, G. (2007) Use of satellite remote sensing data in the mapping of global landslide susceptibility. Natural Hazards, 43, 245–256.

https://earth.esa.int/web/guest/missions/3rd-party-missions/current-missions/deimos-1

Huang, R.Q. and Li, W.L. (2009) Analysis of the geo-hazards triggered by the 12 May 2008 Wenchuan Earthquake. China Bulletin of Engineering Geology and Environment, 68, 363–371.

Huber, S., Younis, M. and Krieger, G. (2010) The TanDEM-X mission: Overview and interferometric performance. International Journal of Microwave and Wireless Technologies, 2, 379-389.

Imhoff, M.L., Lawrence, W.T., Stutzer, D.C. and Elvidge, C.D. (1997) A technique for using composite DMSO/OLS `city lights' satellite data to map urban area''. Remote Sensing of Environment, 361-370.

Janoth, J., Gantert, S., Koppe, W., Kaptein, A. and Fischer, C. (2012) TerraSAR-X2 - Mission overview. Geoscience and Remote sensing Symposium, IEEE International, pp. 217–220.

JAXA (2011) Advanced land observing satellite-2. Available at http://www.jaxa.jp/projects/sat/alos2/index_e.html. Accessed 11 Jun 2013

Joyce, K., Wright, K., Samsonov, S. (2009b) Remote sensing and the disaster management cycle. In: Jedlovec, G. (ed) Advances in geoscience and remote sensing, 48(7). INTECH, pp 317–346.

Joyce, K.E., Belliss, S.E., Samsonov, S.V., McNeill, S.J. and Glassey, P.J. (2009a) A review of the status of satellite remote sensing and image processing techniques for mapping natural hazards and disasters. Progress in Physical Geography, 33, 183–207.

JRC (2012) Global Human Settlement Layer. Available at: http://ghslsys.jrc.ec.europa.eu/ Accessed 14 Jun 2013.

Kaab, A. (2002) Monitoring high-mountain terrain deformation from repeated air- and spaceborne optical data: examples using digital aerial imagery and ASTER data. ISPRS Journal of Photogrammetry and Remote Sensing, 57, 39–52.

Katti, R.V., Thyagarajan, K., Shankara, N.K. and Kiran Kumar, S.A. (2007) Spacecraft technology, special section: Indian space programme. Current Science, 93, 1715–1736.

Kerle, N. (2010) Satellite-based damage mapping following the 2006 Indonesia earthquake—how accurate was it? International Journal of Applied Earth Observation and Geoinformation, 12, 466–476.

Krieger, G., Hajnsek, I., Papathanassiou, K., Eineder, M., Eineder, M., Younis, M., De Zan, F., Prats, P., Huber, S., Werner, M., Fiedler, H., Freeman, A., Rosen, P., Hensley, S., Johnson, W., Veilleux, L., Grafmüller, B., Werninghaus, R., Bamler, R. and Moreira, A. (2009) The Tandem-L Mission Proposal: Monitoring Earth's Dynamics with High Resolution SAR Interferometry. In: Proceedings of the IEEE Radar Conference (RadarCon) (DOI: 10.1109/RADAR.2009.4977077), 1-6.

Langford, M., Higgs, G., Radcliffe, J. and White, S. (2008) Urban population distribution models and service accessibility estimation. Computers, Environment and Urban Systems, 32, 66-80.

Li, M., Cheng, L., Gong, J., Liu, Y., Chen, Z., Li, F., Chen, G., Chen, D. and Song, X. (2008) Post-earthquake assessment of building damage degree using LiDAR data and imagery. Science China Series E: Technology Science, 51, 133–143.

Lindell, M.K. (2000) Politics of hazard mitigation. Natural Hazards Review, 1(2), 73-82.

LinkER (2012) linkER-supporting the implementation of operational GMES services in emergency response. Available at http://www.zki.dlr.de/project/1394. Accessed 14 Jun 2013

Mantovani, F., Soeters, R. and van Westen, C.J. (2013) Remote sensing techniques for landslide studies and hazard in Europe. Geomorphology, 14, 213-225.

Martha, T.R., Kerle, N., van Westen, C.J., Jetten. V. and Kumar, K.V. (2011) Segment optimization and data-driven thresholding for knowledge-based landslide detection by object-based image analysis. IEEE Transactions on Geoscience and Remote Sensing, 49, 4928–4943.

Massonnet, D. and Feigl, K. (1998) Radar interferometry and its application to changes on the earth surface. Reviews of Geophysics, 36, 441–500.

Mennis, J. and Hultgren, T. (2006) Intelligent daysmetric mapping and its application to areal interpolation. Cartography and Geographic Information Science, 33, 179-194.

Mileti, D. (1999) Disasters by Design: A Reassessment of Natural Hazards in the United States. Washington, D.C.: Joseph Henry Press.

Minet, C., Eineder, M., Bamler, R., Hajnsek, I. and Friedrich, A. (2008) Requirements for an L-band SAR-Mission for global monitoring of tectonic activities. USEReST '08, 11–14 November 2008, Naples, Italy.

Moreira, A., Krieger, G., Younis, M., Hajnsek, I., Papathanassiou, K., Eineder, M. and De Zan, F. (2011) Tandem-L: a mission proposal for monitoring dynamic earth processes. In: Geoscience and Remote Sensing Symposium IEEE International, 25–29 July 2011, Vancouver, Canada.

Mueller, M., Segl, K., Heiden, U., Kaufmann, H. (2006) Potential of high-resolution satellite data in the context of vulnerability of buildings. Natural Hazards, 38, 247–258.

NASA (2013) HyspIRI Mission Study Website. Available at http://hyspiri.jpl.nasa.gov/ Accessed 11 Jun 2013

Neer, J.T. (1999) High resolution imaging from space—a commercial perspective on a changing landscape. International Archives of Photogrammetry and Remote Sensing, XXXII(7C2):132-143.

Ostir, K., Veljanovski, T., Podobnikar, T. and Stancic, Z. (2003) Application of satellite remote sensing in natural hazard management: the Mount Mangart landslide case study. International Journal of Remote Sensing, 24, 3983–4002.

Parkinson, C. L. and Greenstone, R. (2000) EOS data products handbook, Volume 2, NASA Goddard Space Flight Center, Greenbelt, Maryland, USA.

Paul, B.K. (2011) Environmental Hazards and Disasters: Contexts, Perspectives and Management. Chichester: Wiley-Blackwell.

Philip, G. (2010) Remote sensing data analysis for mapping active faults in the northwestern part of Kangara Valley, NW Himalaya, India. International Journal of Remote Sensing, 28(21), 4745–4761.

Pittore, M. and Wieland, M. (2019) Towards a rapid probabilistic seismic vulnerability assessment using satellite and ground-based remote sensing. Natural Hazards, doi: 10.1007/s11069-012-0475-z, 2012.

Potere, D. and Schneider, A. (2009) Comparison of global urban maps, In: Global mapping of Human Settlement, In: Gamba, P. and M. Herold (Eds.), Global Mapping of Human Settlements: Experiences, Data Sets, and Prospects, Taylor and Francis, Boca Raton, FL.

Rathje, E.M. and Adams, B.J. (2008) The role of remote sensing in earthquake science and engineering: opportunities and challenges. Earthquake Spectra, 24, 471–492.

Rejaie, A. and Shinozuka, M. (2004) Reconnaissance of Golcuk 1999 earthquake damage using satellite images. Journal of Aerospace Engineering,. 17, 20– 25.

Roessner, S., Wetzel, H.U., Kaufmann, H., Sarnagoev, A. (2005) Potential of satellite remote sensing and GIS for landslide hazard assessment in Southern Kyrgyzstan (Central Asia). Natural Hazards, 35, 395–416.

Rott, H., Nagler, T. (2006) The contribution of radar interferometry to the assessment of landslide hazards. Advances in Space Research 37, 710–19.

SAFER (2011) Services and applications for emergency response. Available at http://safer.emergencyresponse.eu/site/FO/scripts/myFO_accueil.php?lang=EN. Accessed 14 Jun 2013

Sahar, L., Muthukumar, S. and French, P. (2010) Using aerial imagery and GIS in automated building footprint extraction and shape recognition for earthquake risk assessment of urban inventories. IEEE Transactions in Geoscience and Remote Sensing, 48, 3511–3520.

Salvi, S., Stramondo, S., Funning, G.J., Ferretti, A., Sarti, F. and Mouratidis, A. (2012) The Sentinel-1 mission for the improvement of the scientific understanding and the operational monitoring of the seismic cycle. Remote Sensing of Environment, 120, 164–174.

Seifert, F.M. (2009) Improving Urban Monitoring towards a European Urban Atlas. In: Gamba, P., Herold, M. (eds.), Global Mapping of Human Settlement. Experiences, Data sets, and Prospects, 2009, pp. 231-250.

Small, C. and Cohen, J. (2004). Continental physiography, climate, and the global distribution of human population. Current Anthropology, 45(2), 269–277.

Steinborn, W. (2010) The Europe Urban Atlas – supporting city habitability. Available at http://www.sensorsandsystems.com/article/features/6403-the-european-urban-atlas-supporting-city-habitability.html Accessed 14 Jun 2013

Stramondo, S., Moro, M., Tolomei, C., Cinti, F.R. and Doumaz, F. (2005) InSAR surface displacement field and fault modelling for the 2003 Bam earthquake (southeastern Iran). Journal of Geodynamics, 40, 347–353.

Stumpf, A. and Kerle, N. (2011) Object-oriented mapping of landslides using random forests. Remote Sensing of Environment, 115, 2564-2577.

Taubenböck, H., Post, J., Roth, A., Zosseder, K., Strunz, G. and Dech, S. (2008) A conceptual vulnerability and risk framework as outline to identify capabilities of remote sensing. Natural Hazards and Earth System Sciences, 8, 409–420.

Taubenböck. H., Goseberg, N., Setiadi, N., Lämmel, G., Moder, F., Oczipka, M., Klüpfel, H., Wahl, R., Schlurmann, T., Strunz, G., Birkmann, J., Nagel, K., Siegert, F., Lehmann, F., Dech, S., Gress, A., Klein, R. (2009) ‘‘Last-Mile’’ preparation for a potential disaster—interdisciplinary approach towards tsunami early warning and an evacuation information system for the coastal city of Padang, Indonesia. Natural Hazards and Earth System Sciences, 9, 1509–1528.

Taubenböck, H. (2011) The vulnerability of a city—diagnosis from a bird’s eye view. In: Mörner N.A. (ed) The Tsunami threat—research and technology. InTech, Croatia, pp 107–128.

Taubenböck, H., Wurm, M., Netzband, M., Zwenzner, H., Roth, A., Rahman, A., Dech, S. (2011a) Flood risks in urbanized areas – multi-sensoral approaches using remotely sensed data for risk assessment. Natural Hazards and Earth System Science, 11, 431–444.

Taubenböck, H., Esch, T., Felbier, A., Roth, A. and Dech, S. (2011b) Pattern-Based Accuracy Assessment of an Urban Footprint Classification Using TerraSAR-X Data. IEEE Geoscience and Remote Sensing Letters, 8, 278–282.

Taubenböck, H., Esch, T., Felbier, A., Wiesner, M., Roth, A., and Dech, S. (2012a) Monitoring urbanization in mega cities from space. Remote Sensing of the Environment, 117, 162-176.

Taubenböck, H., Roth, A., Esch, T., Felbier, A., Müller, A. and Dech S. (2012b). The vision of mapping the global urban footprint using the TerraSAR-X and TanDEM-X mission. In: Zlatanova, S., Ledoux, H., Fendel, M. and Rumor, M. (eds.), Urban and Regional Management. Taylor & Francis Group, London, 243-251.

Taubenböck, H., Felbier, A., Esch, T., Roth, A. and Dech, S. (2012c) Pixel-based classification algorithm for mapping urban footprints from radar data – a case study for RADARSAT-2. Canadian Journal of Remote Sensing, 38, 211-222.

Theilen-Willige, B. (2010) Detection of local site conditions influencing earthquake shaking and secondary effects in Southwest-Haiti using remote sensing and GIS-methods. Natural Hazards and Earth System Sciences, 10, 1183–1196.

Tierney, K.J., Lindell, M.K. and Perry, R.W. (2001) Facing the Unexpected. Disaster Preparedness and Response in the United States. Washington, D.C. Joseph Henry Press.

Torres, R., Snoeij, P., Geudtner, D., Bibby, D., Davidson, M., Attema, E., Potin, P., Rommen, B., Floury, N., Brown, M., Traver, I.N., Deghaye, P., Duesmann, B., Rosich, B., Miranda, N., Bruno,

C., L'Abbate, M., Croci, R., Pietropaolo, A., Huchler, M. and Rostan, F. (2012) GMES Sentinel-1 mission. Remote Sensing of Environment, 120, 9–24.

Tralli, D.M., Blom, R.G., Zlotnicki, V., Donnellan, A. and Evans, D.E. (2005) Satellite remote sensing of earthquake, volcano, flood, landslide and coastal inundation hazards. Journal for Photogrammetry and Remote Sensing, 59, 185-198.

Trianni, G., Gamba, P. (2009) Fast damage mapping in case of earthquakes using multitemporal SAR data. Journal of Real-Time Image Processing, 4, 195–203.

Tronin, A.A. (1996) Satellite thermal survey—a new tool for the study of seismoactive regions. International Journal of Remote Sensing, 17(8), 1439–1455.

Tronin, A.A. (2006) Remote sensing and earthquakes: A review. Physics and Chemistry of the Earth, 31, 138-142.

Tronin, A.A. (2010) Satellite remote sensing in seismology. A review. Remote Sensing, 2, 124–150.

Tsai, Y.B., Liu, J.Y., Ma, K.F., Yen, H.Y., Chen, K.S., Chen, Y.I. and Lee, C.P. (2006) Precursory phenomena associated with the 1999 Chi–Chi earthquake in Taiwan as identified under iSTEP Program. Physical Chemistry of the Earth, 31, 365–377.

Tsutsui, K., Rokugawa, S., Nakagawa, H., Miyazaki, S., Cheng, C.T., Shiraishi, T. and Yang, S.D. (2007) Detection and volume estimation of large-scale landslides based on elevation-change analysis using DEMs extracted from high-resolution satellite stereo imagery. IEEE Transactions on Geoscience and Remote Sensing, 45, 1681–96.

USGS (2013) Landsat 8. Available at http://landsat.usgs.gov/LDCM_DataProduct.php Accessed 25 Jun 2013

Van Westen, C.J., Castellanos, E. and Kuriakose, S.I. (2008) Spatial data for landslide susceptibility, hazard, and vulnerability assessment. Engineering Geology, 102, 112-131.

Vu, T.T. and Ban, Y. (2010) Context-based mapping of damaged buildings from high-resolution optical satellite images. International Journal of Remote Sensing, 31, 3411–3425.

Vu, T.T., Matsuoka, M. and Yamazaki, F. (2004) LiDAR based change detection of buildings in dense urban areas. In: IEEE international geoscience and remote sensing symposium, September 2004, Anchorage, AK, USA, pp 3413–3416.

Wang, F.T., Zhou, Y., Wang, S.X., Liu, W.L., Wei, C.J. and Han, Y. (2011) Investigation and assessment of damage in earthquake in Yushu, Qinghai based on multi-spectral remote sensing. Spectroscopy and Spectral Analysis, 31, 1047–1051.

Weston, J., Ferreira, A.M.G. and Funning, G.J. (2012) Systematic comparisons of earthquake source models determined using InSAR and seismic data. Tectonophysics, 532–535, 61–81.

Wieland, M., Pittore, M., Parolai, S., Zschau, J., Moldobekov, B. and Begaliev, U. (2012) Estimating building inventory for rapid seismic vulnerability assessment: towards an integrated approach based on multisource imaging. Soil Dynamics and Earthquake Engineering, 36, 70–83.

Wurm, M., Taubenböck, H. and Dech, S. (2009) Urban structuring using multisensoral remote sensing data. In: Proceedings of the Joint Urban Remote Sensing Event, Shanghai, China, 20-22 May 2009. Shanghai: URS/URBAN.

Zeng, J., Zhu, Z.Y., Zhang, J.L., Ouyang, T.P., Qiu, S.F., Zou, Y. and Zeng, T. (2011) Social vulnerability assessment of natural hazards on county-scale using high spatial resolution satellite imagery: a case study in the Luogang district of Guangzhou, South China. Environmental Earth Science, 65, 173–182.